A hybrid classical-quantum transport model for the simulation of Carbon Nanotube transistors

Clément Jourdana, Paola Pietra

A hybrid classical-quantum transport model for the simulation of Carbon Nanotube transistors

C. Jourdana[1] and P. Pietra[2]

[1] Laboratoire Jean Kuntzmann - Université de Grenoble
51 Rue des Mathématiques, BP 53, 38041 Grenoble Cedex 9, France
[2] Istituto di Matematica Applicata e Tecnologie Informatiche - CNR
Via Ferrata 1, 27100 Pavia, Italy
clement.jourdana@imag.fr ; pietra@imati.cnr.it

Abstract

In this paper, we propose a hybrid classical-quantum approach to study the electron transport in strongly confined nanostructures. The device domain is made of an active zone (where quantum effects are strong) sandwiched between two electron reservoirs (where the transport is considered highly collisional). A one dimensional effective mass Schrödinger system is coupled with a drift-diffusion model, both taking into account the peculiarities due to the strong confinement and to the two dimensional transversal crystal structure. Interface conditions are built preserving the continuity of the total current. Self-consistent computations are performed coupling the hybrid transport equations with the resolution of a Poisson equation in the whole three dimensional domain. To illustrate this hybrid strategy, we present simulations of a gate-all-around single-walled Carbon Nanotube Field-Effect Transistor.

Keywords: Quantum-classical coupling, Schrödinger equation, drift-diffusion, interface conditions, effective mass, confined nanostructures, carbon-nanotube FETs.
AMS Subject Classification: 65M60, 65Z05, 78A35, 82D37, 82D80.

1 Introduction

The extreme miniaturization reached in nanoelectronics brings the necessity of using new models to describe accurately the electron transport. Obviously, in the recent semiconductor devices, quantum effects play an important role due to the extremely small dimensions. Nevertheless, some of these quantum effects generally take place in a localized region (for instance, around the double barrier in resonant tunneling diodes or in the active zone in short channel transistors). Since quantum transport simulations are complex and above all computationally expensive, it can be interesting to follow a geometrical hybrid strategy: use a quantum model in regions where quantum effects are strong and couple it to a

model governed by classical mechanics in the rest of the device domain. A hybrid strategy is also motivated by the fact that collisions of charged particles are not easily included into quantum models but they are relevant for the functioning of devices. In Field-Effect Transistors FETs, an active zone is sandwiched between two largely doped regions (Source and Drain) considered as electron reservoirs, and there the transport is expected to be in a highly collisional regime.

In [4], a coupled kinetic-quantum model has been introduced. A Boltzmann equation is used to define the density in the classical zones, instead a Schrödinger equation is chosen to describe the density in the quantum domain. So, the transport in the quantum region is considered ballistic, whereas the classical regions can be highly collisional with an appropriate collision operator. At interfaces, reflection-transmission coefficients are defined to give the boundary conditions of the Boltzmann equation. Inversely, the distribution function is used to construct the quantum density. In that paper, the author proves that the reflection-transmission conditions preserve the current.

Next, in [11], the Boltzmann equation and the reflection-transmission conditions are replaced by a drift-diffusion equation with appropriate interface conditions. These connection conditions are derived from those of [4] through a diffusive approximation and a boundary layer analysis. In [3], the strategy to couple the drift-diffusion Schrödinger system is quite different since the coupling is direct and authors get an analytic expression of the connection conditions by writing the exact continuity of the current at the interfaces. Differently, in [11], due to the diffusion approximation, the continuity of the classical and the quantum current is only preserved up to an order α, where α is the small parameter of the diffusion approximation. We also mention [12] where a hybrid strategy is studied with a quantum drift-diffusion equation. We point out that all these hybrid approaches are different from a "dimensional hybrid coupling" (see [8] e.g.) where electrons are described by a quantum model in the confined direction and a classical drift-diffusion equation along the transport direction.

In this paper, we extend the method of [3] to the framework of strongly confined nanostructure (like nanowires or nanotubes) for which both the quantum transport and the classical collisional transport need new formulations. Indeed, in these structures, the dimension of the transversal cross section is so thin that the transport of charged particles is restricted to the one dimensional longitudinal direction. When the cross–section diameter is below 3 nm, the strong confinement affects the energy band structure and bulk material quantities cannot be used in the simulations (see [13], e.g., and references therein). In particular, the assumption of infinite periodic structure in the wire cross-section, which allows to derive the usual effective mass theorem, is not reasonable anymore. Using an envelope function decomposition, a new effective mass approximation, describing the ballistic transport of electrons in ultra-scaled confined nanostructures, has been obtained in [6]. The model consists of a sequence of one dimensional device dependent Schrödinger equations,

one for each energy band, in which quantities retaining the effects of the confinement and of the transversal crystal structure are inserted. On another hand, a drift-diffusion model which describes the confined diffusive transport, taking into account the interactions of charged particles with phonons, has been derived and analyzed in [18]. It consists of a single macroscopic equation in which atomistic quantities are integrated. The novelty of the present paper is to spatially couple the effective mass model [6] with the nanowire drift-diffusion model [18], preserving the current continuity, as it was announced in the proceeding [7].

Here, the coupling approach requires to take into account different bands, preserving the continuity of the total current. Moreover, while in [11, 3] numerical simulations are performed for a resonant tunneling diode, we consider in this work a strongly confined nanostructure, where self-consistent computations include the resolution, in the whole three dimensional device domain, of a Poisson equation describing a slowly varying macroscopic potential. For an illustration, we have chosen a gate-all-around Carbon Nanotube Field-Effect Transistor (CNTFET).

Carbon Nanotube (CNTs) are rolled-up sheets of graphene. A pair of indices (n, m), called the chiral vector, indicates how the sheet of graphene is wrapped. The CNT is called zig-zag if $m = 0$, armchair if $n = m$, and chiral otherwise. The chirality is crucial in regards to the electronic properties of CNTs. Indeed, if $n - m$ is a multiple of 3, CNTs are metals. Otherwise, they are semiconductors (see [27, 29] e.g.). Semiconducting CNTs have emerged as promising candidates to build the future FETs because of their superior electrical characteristics over usual FETs (see [23, 26, 21, 14, 19] and references therein for details). The modeling of such devices is very important in order to predict their behavior, to access their performance limits and to design new configurations. That is why we propose in this paper a hybrid approach that allows for computationally efficient numerical simulations, that can be used in a device design framework.

The paper is organized as follows. In Section 2, we present the zig-zag (10,0) single-walled carbon nanotube used all along this article to illustrate the hybrid approach. We also define the relevant physical quantities that retain the atomistic description of the strongly confined cross-section, recalling the model derived in [6] . In Section 3, we describe the geometrical coupling, detailing the equations in the classical regions (introduced in [18]), those in the quantum zone (obtained in [6]) and explaining the derivation of interface conditions. We also present the self–consistent formulation which consists in coupling the 1D transport equations with a 3D Poisson equation. Section 4 describes the iterative algorithm and the numerical issues. Finally, the numerical experiments are collected in Section 5. After a description of the gate-all-around CNTFET, we compare the hybrid approach with the full drift-diffusion model [18] and the full quantum one [6]. In particular, we discuss the impact of the electron mobility and the influence of interface positions.

2 Preliminaries

We are interested in simulations of the electron transport in a semiconducting carbon nanotube. More precisely, we consider a gate-all-around CNTFET. To fix ideas, we describe here the device that will be simulated in the results presented in Section 5. It is however clear that the model and the numerical algorithm can be applied to general strongly confined nanostructures (such as silicon nanowires or different CNTs), with different gate geometries. We consider a (10,0) zig-zag single-walled CNT (see Fig.1 for a representation of atom positions), surrounded by a layer of dielectric acting as an insulator of 1.4 nm thickness. The carbon atoms are placed on a circle of 0.78 nm diameter.

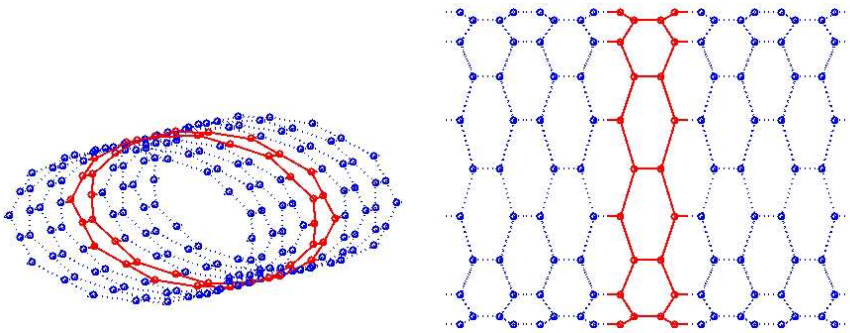

Figure 1: 3D (left) and 2D (right) representation of atom positions in a (10,0) "zig-zag" carbon nanotube. The solid red part corresponds to the atoms in a unit cell.

In [6], a novel quantum effective mass model has been derived by performing an asymptotic process which consists in using an envelope function decomposition to obtain a new effective mass approximation (see also [2] for a similar approach for 3D periodic crystals). We recall it briefly here. Let us consider an infinite wire defined in a physical domain $\mathbb{R} \times \omega_\epsilon$, where ϵ is the typical spacing between lattice sites. As starting point, the transport is described by a scaled Schrödinger equation in $\mathbb{R} \times \omega_\epsilon$ containing a potential $W_{\mathcal{L}}$ generated by the crystal lattice, fast oscillating in the scale defined by the crystal spacing, and a slowly varying external potential V

$$\begin{cases} i\hbar\partial_t\psi^\epsilon = -\frac{\hbar^2}{2m_e}\Delta\psi^\epsilon + \frac{1}{\epsilon^2}W_{\mathcal{L}}\left(\frac{x}{\epsilon}, \frac{z}{\epsilon}\right)\psi^\epsilon + V\left(x, \frac{z}{\epsilon}\right)\psi^\epsilon & (x,z) \in \mathbb{R} \times \omega_\epsilon, \\ \psi^\epsilon = 0 \text{ for } z \in \partial\omega_\epsilon. \end{cases} \tag{2.1}$$

Here, $\hbar$ is the reduced Planck constant and m_e is the electron mass. Since the 2D cross-section ω_ϵ comprises few ions, $W_{\mathcal{L}}$ is considered periodic only in the longitudinal x-direction (transport direction) and the variable z of the transverse section can be considered as fast variable, rescaled as $z' = \frac{z}{\epsilon}$. Denoting by ω the scaled cross–section, we consider the following Bloch-type problem (with a quasimomentum equal to 0) in the 3D cell $\mathcal{U} =$

$(-1/2, 1/2) \times \omega$

$$\begin{cases} -\frac{\hbar^2}{2m_e}\Delta\chi_n + W_{\mathcal{L}}\chi_n = E_n\chi_n, \\ \chi_n(y, z') = 0 \ \text{ on } \partial\omega, \quad \chi_n \ \text{ 1-periodic in } y, \\ \int_{\mathcal{U}} |\chi_n|^2 dy dz' = 1. \end{cases} \tag{2.2}$$

Here y denotes the transport variable in the cell. The peculiarity of the strongly confined structure is reflected in the choice of the unit cell problem (2.2) of Bloch type. We point out that this unit cell $\mathcal{U}$ comprises the entire cross–section of the nanostructure (for instance, in the case of the (10,0) carbon nanotube structure, it contains all the red atoms highlighted in Fig.1 by the solid lines that connect them). Thus, the eigenvectors depend on the device under consideration, for instance on the device geometry, on the number of atoms, on the chirality, and so on. Moreover, the homogeneous Dirichlet condition imposes confinement in the transverse directions, while periodicity is considered only in the transport direction. Consequently, the eigenvectors are 3D quantities but the Brillouin zone and the associated energy bands are one dimensional.

The asymptotic process [6], by using the functions defined in (2.2) as basis for the envelope function decomposition, allows to average out not only the lattice potential, but also the lateral dimension. The quantum electron transport is then modeled by an infinite set of Schrödinger equations, one for each band, where relevant averaged quantities, based on the Bloch functions, are incorporated. In particular, in the non–degenerate case (i.e. assuming that all the eigenvalues of the problem (2.2) are simple, as it will be considered all along this paper), the equations are decoupled and have the form

$$\imath\hbar\partial_t h_n(t, x) = -\frac{\hbar^2}{2m_n^*}\partial_{xx} h_n(t, x) + V_{nn}(x) h_n(t, x), \qquad x \in \mathbb{R}. \tag{2.3}$$

The $n-th$ band effective mass m_n^* is defined by

$$\frac{m_e}{m_n^*} = 1 - \frac{2\hbar^2}{m_e} \sum_{n' \neq n} \frac{P_{nn'} P_{n'n}}{E_n - E_{n'}}, \qquad \text{where} \qquad P_{nn'} = \int_{\mathcal{U}} \partial_y \chi_{n'}(y, z') \chi_n(y, z')\, dy dz'. \tag{2.4}$$

Also, the effective potential is given by

$$V_{nn}(x) = \int_\omega V(x, z') g_{nn}(z')\, dz', \qquad \text{with} \qquad g_{nn}(z') = \int_{-1/2}^{1/2} |\chi_n(y, z')|^2\, dy. \tag{2.5}$$

For the degenerate case, we simply recall that the equations corresponding to the same eigenvalue are coupled through the potential term, while the kinetic part is diagonal. We refer to [6] for details.

To complete the description of the nanostructure under consideration, in Fig.2 we present the energy bands. They are calculated solving in the 3D cell $\mathcal{U}$ the eigenvalue problem for the fibered Hamiltonian

$$H_{\mathcal{L}}(k) = -\frac{\hbar^2}{2m_e}\Delta - i\frac{\hbar^2}{m_e} k \partial_y + \frac{\hbar^2 k^2}{2m_e} + W_{\mathcal{L}} \tag{2.6}$$

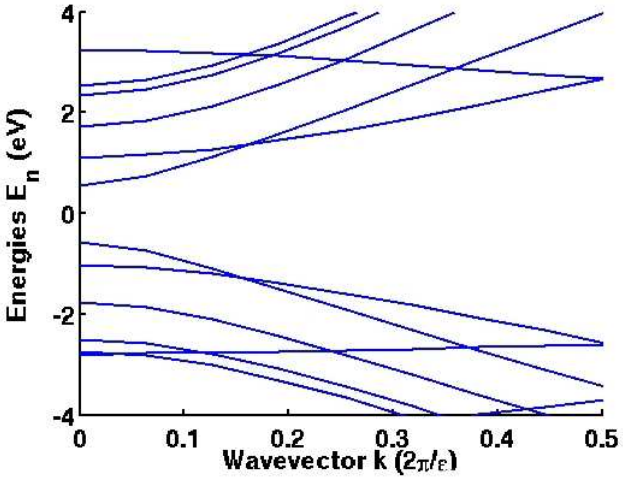

Figure 2: Energy bands obtained for a (10,0) carbon nanotube.

for different wavevector k and with $W_{\mathcal{L}}$ as the pseudopotential given in [24]. Piecewise linear finite elements on prisms with an appropriate non-uniform mesh have been used (see Fig.6 for an illustration of the 2D cross-section mesh). Fig.2 is in good accordance with the results presented in Fig.4 in [24] for the same choice of pseudopotential. Notice that similar results can be provided by different methods (for instance using tight-binding models [10, 28]). We point out that the model described in [6] does not rely only on the knowledge of the energy bands. This is only the first step in the construction of the effective mass model. The important and novel issue is the link between the 1D transport equations and the 3D confined nanostructure, incorporating the atomistic information of the 2D cross-section by means of the functions g_{nn}'s. In actual computations, we only solve problem (2.2), which corresponds to $H_{\mathcal{L}}(0)$, in order to obtain the eigenvalues E_n, the effective masses m_n^* and the functions g_{nn}'s.

In Figs.3 and 4, we present the g_{nn}'s corresponding to the three first conduction bands for the (10,0) carbon nanotube structure, showing that the g_{nn}'s retain information about the confinement and the cross-section structure. These same averaged quantities enter in the diffusive model derived in [18] and used in the following of the paper where we propose a hybrid strategy coupling the fully quantum model [6] with the diffusive one [18].

3 Electron transport with a hybrid strategy

In this paper, we consider the CNTFET described above. In the transport direction we consider a channel region sandwiched between largely doped Source and Drain regions. It is defined by the bounded domain $\Omega = (x_L, x_R) \times \omega_\epsilon$, where (x_L, x_R) is the transport domain and ω_ϵ is the two dimensional strongly confined cross–section. The novelty is that

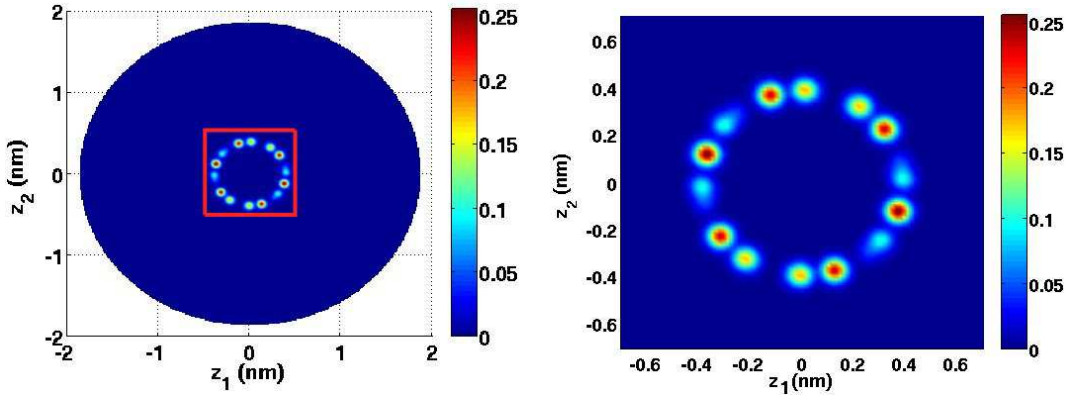

Figure 3: $g_{nn}(z)$ for the first conduction band.

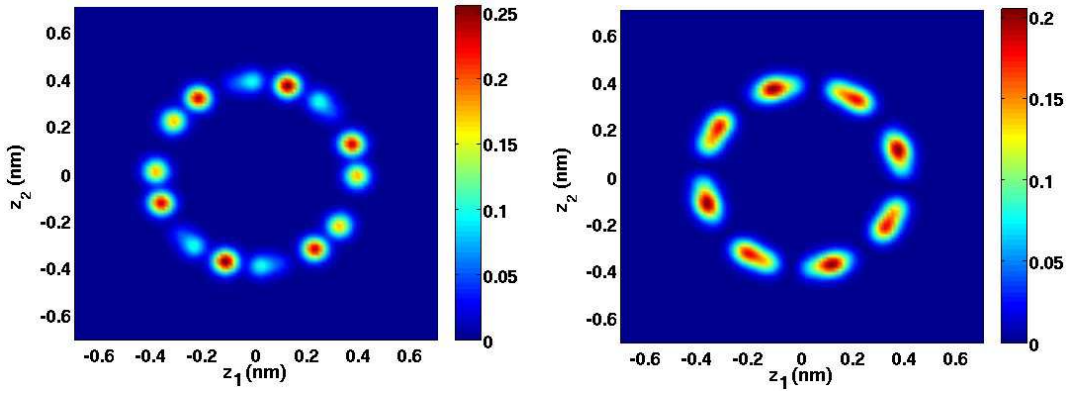

Figure 4: $g_{nn}(z)$ for the second (left) and the third (right) conduction band.

we present a hybrid strategy to couple, spatially in the transport direction, the Schrödinger system (derived and tested numerically on a "toy" problem in [6]) with the drift-diffusion model (introduced and analyzed in [18]). So, we assume that the device domain in the transport direction x is divided into a quantum zone $Q = (x_{I_1}, x_{I_2})$, with $x_L < x_{I_1} < x_{I_2} < x_R$ and a classical zone $C = (x_L, x_R) \backslash Q$. The different regions of the domain (x_L, x_R) are illustrated in Fig.5.

We assume at this point that the electrostatic potential V is given (and consequently so is the $n-th$ band effective potential V_{nn}). We write first the transport equations in the classical regions, as well as the equations in the quantum region. Afterward, we describe the interface conditions which preserve the continuity of the total current between the classical and the quantum domains. Finally, we present the self-consistent Poisson equation.

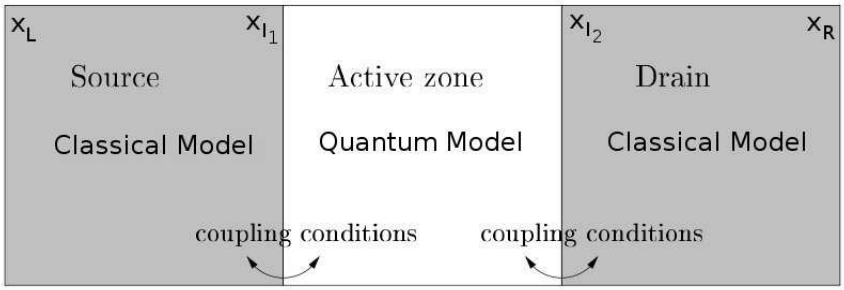

Figure 5: Schematic representation of hybrid model regions.

3.1 The classical region

The classical transport is described by the diffusive model for confined nanostructures which has been derived and analyzed in [18]. Here we consider that stationary nanowire-drift-diffusion model on the disconnected domain C

$$\frac{d}{dx}J_C(x) = 0, \tag{3.1}$$

where the classical current is written in terms of the quasi-Fermi energy φ as

$$J_C(x) = -\mu(x)\ \partial_x\varphi(x)\ F\big(V_s(x) - \varphi(x)\big). \tag{3.2}$$

Here μ is the electron mobility coefficient which, in the particular case of a constant scattering kernel in the collision operator that gives rise to this diffusive model, is defined by

$$\mu(x) = m_e\ \widetilde{\mu} \sum_{n=1}^{+\infty} \frac{e^{-\left(E_n + V_{nn}(x)\right)/(k_B T)}}{m_n^* \sum_{m=1}^{+\infty} e^{-\left(E_m + V_{mm}(x)\right)/(k_B T)}}, \tag{3.3}$$

where the constant $\widetilde{\mu} = \frac{q\tau}{m_e}$, with τ denoting the relaxation time, can be interpreted as the low field mobility constant. We notice that the mobility coefficient $\mu(x)$ exhibits some spatial variations due to the variations of V_{nn}. An analogy can be seen with the electric field dependent mobility (see i.e. [25, 22]). Moreover, V_s is the effective potential defined by

$$V_s(x) = -k_B T \ln \mathcal{Z}(x) \quad \text{with} \quad \mathcal{Z}(x) = \sum_{n=1}^{+\infty} e^{-\left(E_n + V_{nn}(x)\right)/(k_B T)}, \tag{3.4}$$

where k_B is the Boltzmann constant and T is the lattice temperature. Finally, we recall that the 1D density is defined by

$$N_s = F(V_s - \varphi), \tag{3.5}$$

which, in the case of the Boltzmann statistics, is defined by

$$F(s) = n_i e^{-s/(k_B T)}, \tag{3.6}$$

where n_i is the 1D intrinsic density. We point out that the choice to use the quasi-Fermi energy formulation is crucial, motivated by the fact that we want to find an analytic expression of the interface conditions, as we will explain in the following.

Dirichlet conditions are given at the boundary, imposing quasi–neutrality between the density N_s and the background ion density N_D. More precisely, denoting by x_b the abscissa at the boundary ($b = L$ or $b = R$), we take

$$N_s(x_b) = \int_{\omega_\epsilon} N_D(x_b, z)dz, \tag{3.7}$$

where N_D is the prescribed 3D doping density. For the Boltzmann statistics (3.6), the boundary condition (3.7) leads to

$$\varphi(x_b) = k_B T \ln\left(\frac{\int_{\omega_\epsilon} N_D(x_b, z)dz}{n_i}\right) + V_s(x_b). \tag{3.8}$$

Finally, the two disconnected classical zones are connected by means of the conditions

$$J_C(x_{I_1}) = J_C(x_{I_2}) = h(\varphi(x_{I_1})) - h(\varphi(x_{I_2})), \tag{3.9}$$

which relate the quasi-Fermi energy φ at the two interface points. If h is a real-valued and monotonously increasing function, then system (3.1)-(3.2) with boundary conditions (3.8)-(3.9) is well posed (see [3] and references therein). We will determine the function h in the following subsections, by means of the quantum expression of the current. Here we notice that without applied voltage, $\varphi(x_{I_1}) = \varphi(x_{I_2})$ and thus $J_C = 0$. We also see that $\varphi(x_{I_1}) > \varphi(x_{I_2})$ gives a positive current and inversely.

Finally, in preparation for self-consistent computations, from N_s we need to define a charge density for each band. We do so, recalling that the starting point of [18] to obtain the nanowire-drift-diffusion model (3.1),(3.2) is a sequence of decoupled Boltzmann equations, one for each band, and that the approximate solution of the $n-th$ band kinetic equation, up to order 1 in the scaled mean free path parameter, is given by the distribution function

$$g_n(x,k) = N_s(x)\frac{\hbar}{\sqrt{2\pi m_n^* k_B T}\ \mathcal{Z}(x)}\ e^{-(\frac{\hbar^2 k^2}{2m_n^*} + E_n + V_{nn}(x))/(k_B T)}. \tag{3.10}$$

Using (3.5), (3.6) and (3.4), the previous formula takes the form

$$g_n(x,k) = \frac{n_i \hbar}{\sqrt{2\pi m_n^* k_B T}}\ e^{-\left(\frac{\hbar^2 k^2}{2m_n^*} + E_n + V_{nn}(x) - \varphi(x)\right)/(k_B T)}. \tag{3.11}$$

Proceeding as in [18], we integrate (3.11) over k and we obtain

$$N_C^n(x) = F\big(V_s(x) - \varphi(x)\big)\frac{e^{-\left(E_n + V_{nn}(x)\right)/(k_B T)}}{\mathcal{Z}(x)}. \tag{3.12}$$

We notice that the sum over all the bands gives the density N_s.

3.2 The quantum region

The quantum transport in Q is given by the sequence of Schrödinger equations (3.13). The system is considered as an open system in (x_{I_1}, x_{I_2}), with Transparent Boundary Conditions supplementing the equations (see [20], [5], e.g.). To fix ideas, we detail the case $V_{nn}(x_{I_1}) \geq V_{nn}(x_{I_2})$. For each band and for each wave vector k, we consider the following stationary Schrödinger equation

$$-\frac{\hbar^2}{2m_n^*}\partial_{xx}\psi_n^k(x) + V_{nn}(x)\psi_n^k(x) = \mathcal{E}_{n,k}\psi_n^k(x), \quad \text{in } Q, \tag{3.13}$$

where

$$\mathcal{E}_{n,k} = \begin{cases} \mathcal{E}_{n,k}^+ = \frac{\hbar^2 k^2}{2m_n^*} + V_{nn}(x_{I_1}) & \text{if } k > 0, \\ \mathcal{E}_{n,k}^- = \frac{\hbar^2 k^2}{2m_n^*} + V_{nn}(x_{I_2}) & \text{if } k < 0. \end{cases}$$

Defining the coefficients

$$p_n^{\pm}(k) = \sqrt{\hbar^2 k^2 \mp 2m_n^*(V_{nn}(x_{I_2}) - V_{nn}(x_{I_1}))}, \tag{3.14}$$

the TBCs are written for $k > 0$ as

$$\partial_x\psi_n^k(x_{I_1}) + ik\psi_n^k(x_{I_1}) = 2ik \quad \text{and} \quad \hbar\partial_x\psi_n^k(x_{I_2}) = ip_n^+(k)\psi_n^k(x_{I_2}), \tag{3.15}$$

and for $k < 0$, we have

$$\partial_x\psi_n^k(x_{I_2}) + ik\psi_n^k(x_{I_2}) = 2ik \quad \text{and} \quad \hbar\partial_x\psi_n^k(x_{I_1}) = -ip_n^-(k)\psi_n^k(x_{I_1}). \tag{3.16}$$

The reflection and transmission amplitudes $r_n(k)$ and $t_n(k)$ of the wave functions are determined by

$$r_n(k) = \frac{1}{2}\psi_n^k(x_{I_1}) + \frac{i}{2k}\partial_x\psi_n^k(x_{I_1}) \quad \text{and} \quad t_n(k) = \psi_n^k(x_{I_2}) \quad \text{for} \quad k > 0,$$

$$r_n(k) = \frac{1}{2}\psi_n^k(x_{I_2}) + \frac{i}{2k}\partial_x\psi_n^k(x_{I_2}) \quad \text{and} \quad t_n(k) = \psi_n^k(x_{I_1}) \quad \text{for} \quad k < 0.$$

Finally, we define the reflection coefficients as $R_n(k) = |r_n(k)|^2$ and the transmission coefficients $T_n(k)$, corresponding to the proportion of incident electrons which are transmitted, as

$$T_n(k) = \begin{cases} \frac{p_n^+(k)}{\hbar k}|t_n(k)|^2 & \text{if } k > 0, \\ -\frac{Re\left(p_n^-(k)\right)}{\hbar k}|t_n(k)|^2 & \text{if } k < 0. \end{cases} \tag{3.17}$$

The transmission coefficients have the following properties

$$T_n(k) + R_n(k) = 1 \qquad \text{for all } k \in \mathbb{R}, \tag{3.18}$$

$$T_n(k) = T_n\Big(-\frac{p_n^+(k)}{\hbar}\Big) \qquad \text{for all } k > 0, \tag{3.19}$$

$$T_n(k) = T_n\Big(\frac{p_n^-(k)}{\hbar}\Big) \qquad \text{for all } \hbar k < -p_n^+(0), \tag{3.20}$$

$$T_n(k) = 0 \qquad \text{for all } -p_n^+(0) < \hbar k < 0, \tag{3.21}$$

Next, the 1D density carried by the n-th band N_{1D}^n in the Q region is given by superimposing the densities of states injected from the reservoirs, that is

$$N_Q^n(x) = \int_{\mathbb{R}} \phi_n(k)|\psi_n^k(x)|^2 dk, \qquad x \in Q, \tag{3.22}$$

where $\phi_n(k)$ is a given statistical function which characterizes the electron injection from reservoirs and whose choice will be discussed in the next subsection.

Finally, the current is defined by

$$J_Q(x) = \sum_{n=1}^{+\infty} J_Q^n(x), \tag{3.23}$$

where the n^{th} band current is given by

$$J_Q^n(x) = \frac{q\hbar}{m_n^*} \int_{\mathbb{R}} \phi_n(k) \Im\Big(\overline{\psi_n^k(x)} \partial_x \psi_n^k(x)\Big) dk, \qquad x \in Q. \tag{3.24}$$

It can be easily seen that the current does not depend on x. Furthermore, using the TBCs of the Schrödinger equation (3.15) and (3.16), as well as the expression of the transmission coefficients (3.17) with the properties (3.18)-(3.21), J_Q^n can be expressed in the following form

$$J_Q^n = \frac{q\hbar}{m_n^*} \int_0^{+\infty} kT_n(k)\Big(\phi_n(k) - \phi_n(-\frac{p_n^+(k)}{\hbar})\Big) dk. \tag{3.25}$$

3.3 The interface conditions

So far, we still did not make an explicit choice for the monotone function h in (3.9) and for the statistical function in (3.22) and in (3.25). Our choice will lead to the definition of h in terms of the quantum current J_Q.

As statistical function in (3.22) and in (3.25) we choose the distribution function related to the diffusive model at the interface, (assuming, for the moment, that the quasi-Fermi energy φ is known). More precisely, we take

$$\phi_n(k) = \begin{cases} g_n(x_{I_1}, k) & \text{if } k > 0, \\ g_n(x_{I_2}, k) & \text{if } k < 0, \end{cases}$$

with g_n defined in (3.11). Introducing f_n as

$$f_n(s) = \frac{n_i \hbar}{\sqrt{2\pi k_B T m_n^*}} e^{-s/(k_B T)}, \tag{3.26}$$

and observing that $\mathcal{E}^-_{n,-p_n^+(k)/\hbar} = \mathcal{E}^+_{n,k}$, we can write (3.25) as

$$J_Q^n = \frac{q\hbar}{m_n^*} \int_0^{+\infty} kT_n(k) f_n(E_n + \mathcal{E}^+_{n,k})\Big(e^{\varphi(x_{I_1})/(k_B T)} - e^{\varphi(x_{I_2})/(k_B T)}\Big) dk. \tag{3.27}$$

Notice that the term containing the quasi-Fermi energy variables enters (3.27) as a multiplication factor, and this is crucial to write the interface conditions in an explicit way.

With the definition

$$h(\varphi) = \sum_{n=1}^{+\infty} \frac{q\hbar}{m_n^*} \int_0^{+\infty} kT_n(k) f_n\Big(E_n + \mathcal{E}_{n,k}^+ - \varphi\Big) dk. \tag{3.28}$$

we obtain immediately from (3.23) and (3.27) that

$$J_Q = h(\varphi(x_{I_1})) - h(\varphi(x_{I_2})).$$

We point out that the function $h(s)$ is monotone increasing since $f_n(s)$ is monotone decreasing. The function h can be expressed explicitly, by means of

$$h(\varphi) = \Theta^{-1} e^{\varphi/(k_B T)}, \tag{3.29}$$

where Θ is a positive number defined by

$$\Theta^{-1} = \sum_{n=1}^{+\infty} \frac{q\hbar}{m_n^*} \int_0^{+\infty} kT_n(k) f_n(E_n + \mathcal{E}_{n,k}^+) dk. \tag{3.30}$$

Consequently, imposing $J_C = J_Q$, we obtain the final interface conditions

$$J_C(x_{I_1}) = J_C(x_{I_2}) := J_C, \tag{3.31}$$

and

$$e^{\varphi(x_{I_1})/(k_B T)} - e^{\varphi(x_{I_2})/(k_B T)} = \Theta J_C. \tag{3.32}$$

Remark 3.1. *The interface conditions (3.31) and (3.32) have been constructed preserving the continuity between the classical and the quantum current, which is the relevant physical property. It is however clear that continuity of the charge density is not assured.*

3.4 Self-consistent formulation

In order to define the self–consistent electrostatic potential, a 3D charge density is required. First of all, the 1D charge density of the hybrid model in the $n-th$ band N_{1D}^n is defined by

$$N_{1D}^n(x) = \begin{cases} N_Q^n(x) & \text{for } x \in Q, \\ N_C^n(x) & \text{for } x \in C, \end{cases}$$

where N_Q^n and N_C^n are given in (3.22) and (3.12), respectively. Then, as in [6] and in [18], the transformation from the one dimensional transport direction to the entire nanostructure is done by means of the (properly scaled) quantities g_{nn}'s (2.5). It leads to

$$\rho(x,z) = \sum_{n\in\mathbb{N}} N_{1D}^n(x) g_{nn}^\epsilon(z) \qquad (x,z) \in (x_L, x_R) \times \omega_\epsilon, \tag{3.33}$$

where $g^{\epsilon}_{nn}(z) = \frac{1}{\epsilon^2} g_{nn}(\frac{z}{\epsilon})$. Finally, the transport equations are coupled with the following Poisson equation for the electrostatic potential V_P

$$-\nabla\big(\epsilon_r(z)\nabla V_P(x,z)\big) = \frac{q}{\epsilon_0}\Big(N_D(x,z) - \rho(x,z)\Big), \qquad (x,z) \in (x_L, x_R) \times \omega_\epsilon, \qquad (3.34)$$

where q is the elementary charge, ϵ_0 the permittivity in vacuum, ϵ_r the relative permittivity and N_D the prescribed doping density. Equation (3.34) is then supplemented by boundary conditions at Source and Drain contacts, at the gate contact and at the insulating boundaries, for which we refer to [6], Section 5.5. Then, V in (2.5) is given by $V = -qV_P$.

4 Algorithm approach

We describe here the numerical issues related to the solution of the coupled 1D transport equations with the 3D Poisson equation, once the atomistic quantities are computed on the unit cell, by means of the solution of the eigenvalue problem (2.2). The 3D mesh for the Poisson equation consists of prisms, with a 2D cross–section triangular mesh as in Fig.6 and with 151 equally spaced discretization points in the longitudinal direction (discretization step: 0.2 nm). We point out that the 2D cross–section mesh is the same as the one used for the solution of the eigenvalue problem (obviously the 3D domain is different), so that the functions $g_{nn}(z')$ are incorporated in the Poisson problem without resorting to any interpolation. Finally, due to the highly oscillatory behavior of the wave functions with high energy, a fine mesh size is required for the 1D transport computations. We take 751 equally spaced discretization points (discretization step: 0.04 nm).

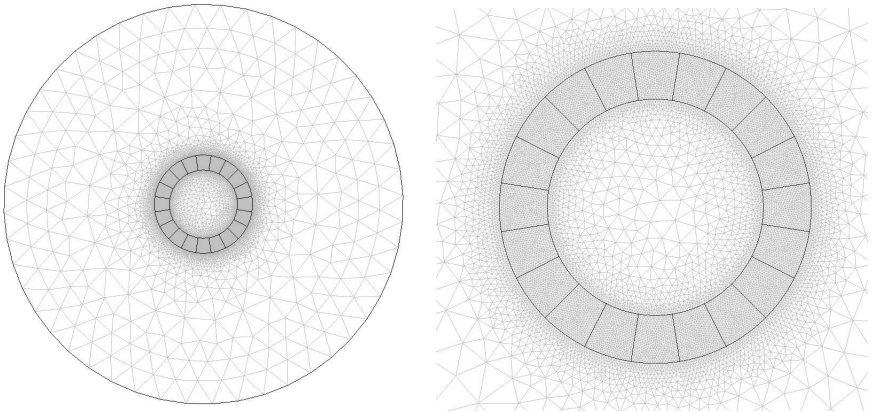

Figure 6: Mesh of the circular cross–section : entire mesh (left) and zoom of the carbon domain (right).

For a given gate voltage V_G, we first consider the whole system for zero applied Drain-Source voltage V_{DS} and then we increment V_{DS} step by step. Finally, this procedure is repeated for different gate voltage V_G.

Because of the highly nonlinear coupling between the density and the potential equations, the inner iteration procedure is done by an iterative method of Gummel type [15]. We detail here the different steps of one iteration of this Gummel type algorithm.

1. Let V_P^{old} be a given approximate electrostatic potential in the finite element space of piecewise linear polynomials on the prismatic mesh described above.

2. We define the potential energy $V = -qV_P^{old}$ and compute the quantities V_{nn} (2.5), V_s (3.4) as well as μ (3.3).

3. For each band n and each wave vector k, we solve on Q the Schrödinger equations (3.13), with the TBCs (3.15). A single equation for $k > 0$ is first rewritten, by means of the transformation $\psi_n^k(x) = 2ik\Psi_n^k(x)/[\partial_x\Psi_n^k(x_{I_1}) + 2ik\Psi_n^k(x_{I_1})]$, as an initial value problem. Then, it is discretized with a Crank–Nicolson scheme, which is a conservative scheme and avoids numerical dissipation for large k's. The negative wave vector case is treated analogously. Then, the transmission coefficients T_n (3.17) are obtained and, subsequently, the number Θ (3.30) is computed.

4. We solve the stationary drift-diffusion equation (3.1) on C with the boundary conditions (3.8) and the two connection conditions (3.31) and (3.32). The non–linear equation (3.1) is discretized by means of a mixed finite element scheme in hybrid form [1], which, after the static condensation process, takes the form

$$-D_0^j\varphi_{j-1} + \big(D_0^j + D_0^{j+1}\big)\varphi_j - D_0^{j+1}\varphi_{j+1} = 0, \tag{4.1}$$

   where φ_j denotes the value of the approximate quasi–Fermi energy φ_h at the discretization point x_j. The coefficients D_0 are given by

$$D_0^j = D_0^j(\varphi_h) = -n_i\frac{\mu_j + \mu_{j-1}}{2}e^{\left(\frac{\varphi_j+\varphi_{j-1}}{2k_BT}\right)}/\mathcal{I}(V_s/k_BT), \tag{4.2}$$

   where μ_j are the values of the given (within this iteration step) functions $\mu(x)$ at x_j, and $\mathcal{I}(u) = \int_{x_j}^{x_{j+1}} e^{u(x)}dx$, which here can be computed exactly, because the (given) V_s is piecewise linear.

   The (globally constant) current is then given by

$$J_j = D_0^j * \big(\varphi_j - \varphi_{j-1}\big). \tag{4.3}$$

   The non–linear equation (4.1) is solved by means of a Newton algorithm. We obtain the quasi-Fermi energy φ. We recall that mixed finite elements schemes for the drift–diffusion in the quasi-Fermi energy formulation have been used in [16, 17].

5. We compute the classical density on each band N_C^n (3.12), and, using $\varphi(x_{I_1})$, $\varphi(x_{I_2})$ in (3.22), the quantum density on each band N_Q^n . Finally, we compute the three dimensional density ρ (3.33).

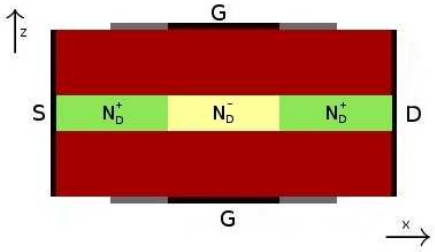

Figure 7: Longitudinal section of the CNTFET.

6. We solve the 3D Poisson equation using piecewise linear finite elements on the prismatic mesh described above, modified according to the Gummel iteration algorithm, as in [9], that is

$$-\nabla\big(\epsilon_r(z)\nabla V_P^{new}\big) = \frac{q}{\epsilon_0}N_D - \frac{q}{\epsilon_0}\rho[V_P^{old}]\Big(1 + \frac{q}{k_BT}(V_P^{new} - V_P^{old})\Big), \quad \text{in } (x_L, x_R)\times\omega_\epsilon. \tag{4.4}$$

7. We repeat the last five steps until the quantity $\|V_P^{old} - V_P^{new}\|_{L^\infty}$ becomes sufficiently small. Once the convergence is reached, we increment the applied Drain-Source bias V_{DS} and start a new iteration. For the device presented in Section 5, the convergence algorithm is not very sensitive to the size of the V_{DS} increment, since the Current–Voltage characteristics do not present a stiff behavior. We numerically found that a uniform increment step equal to 0.02 V is a reasonable choice. Moreover, as usual for MOS devices, the number of Gummel iterations increases for large gate voltages V_G (see Table 1), but convergence is still reached with the same V_{DS} increment.

5 Numerical results

Numerical simulations are carried out for a Carbon Nanotube Field-Effect Transistor CNTFET. A section along the transport direction (x-axis) is presented in Fig.7. It contains a (10,0) zig-zag single-walled CNT (see Fig.1) surrounded by a layer of dielectric SiO_2 ($\epsilon_{r,ox} = 3.9$) of 1.4 nm thickness (represented in red) acting as an insulator. The relative permittivity of a CNT is a device dependent quantity, that here has been taken as $\epsilon_{r,c} = 13$. The transport direction is composed of a 10 nm active zone, with a doping concentration $N_D^- = 10^{21}\ m^{-3}$, sandwiched between a 10 nm Source region and a 10 nm Drain region, with large doping ($N_D^+ = 10^{27} m^{-3}$). Finally, a Gate is imposed all-around the transversal structure to modulate the number of free electrons. In the sequel, two different cases will be illustrated. In the first case (non-overlap case), the gate is positioned in correspondence to the active zone (black G in Fig.7), whereas in the overlap case, the gate is 20 nm long and it acts also on a part of Source and Drain regions (black+grey G).

In the present simulations, the hybrid interfaces are located at $x_{I_1} = 10$ nm and $x_{I_2} = 20$ nm, which correspond to the doping discontinuities. In Subsection 5.4, we will discuss how the interface position affects the device behavior. The transport-Poisson problem is only solved for the 9 first conduction bands. This choice is widely sufficient as we will see in Subsection 5.5. Among these 9 modes, there are degenerate eigenvalues. Nevertheless, the off-diagonal potentials V_{nm} (analogous of (2.5)) are virtually zero and it is reasonable to neglect the coupling of these bands. It amounts to assume that all the eigenvalues are simple.

5.1 The electron mobility

First, we would like to make some comments about the electron mobility constant $\widetilde{\mu}$ (3.3). For strongly confined structures, this is a device dependent physical parameter and a well established value is not found in the literature. Therefore, we discuss how different choices affect our simulations with the hybrid strategy. In Fig.8, the output current-voltage characteristics (for the fixed gate voltage $V_G = -0.1$ V) are presented for different mobility constants $\widetilde{\mu}$. The right picture shows the current value for a fixed applied voltage $V_{DS} = 0.2$ V (which corresponds to a saturation regime).

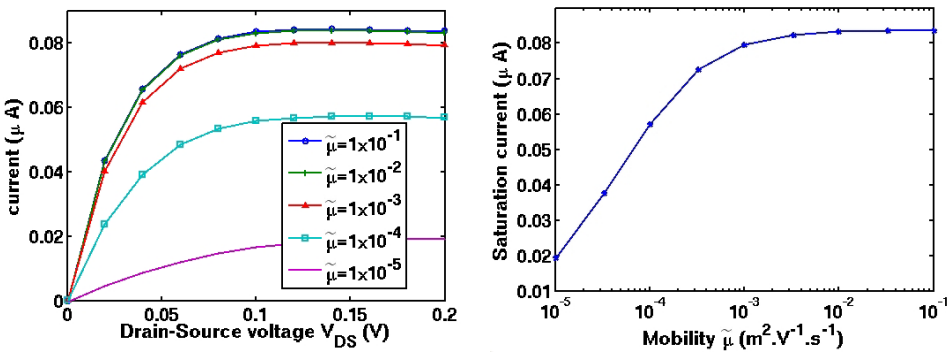

Figure 8: Mobility influence on the current-voltage characteristics (left) and the saturation current (right) with the hybrid approach for $V_G = -0.1$ V.

This behavior is peculiar of the hybrid approach. While solving the transport problem with the drift-diffusion model in the entire longitudinal domain provides a current which is proportional to the mobility constant, in the hybrid case we observe that for mobilities larger than $10^{-3}\ m^2\,V^{-1}\,s^{-1}$ the current is virtually not modified. This means that the quantum model in the channel region is predominant in the computation of the electron transport. On the contrary, for smaller mobilities, the hybrid model is able to capture the limited transport behavior due to the large number of collisions.

In order to choose the value for $\widetilde{\mu}$ for our simulations, we compare the current-voltage characteristics for the three possible models (full drift-diffusion model, full quantum model

and hybrid approach). It turns out that $\widetilde{\mu} = 0.5 \times 10^{-4}\ m^2\, V^{-1}\, s^{-1}$ is a reasonable choice. Indeed, with this choice (see Fig.9), the drift–diffusion current is much smaller than the two others and the quantum current is higher than the hybrid one. This means on one hand that ballistic quantum effects are well considered in the active zone. On the other hand, electron-phonon collisions are taken into account in the reservoirs. Moreover, since the hybrid current is quantitatively closer to the quantum one, the quantum ballistic effects are here considered predominant with respect to the collisional effects, which is preferable in modeling electron transport in a strongly confined structure.

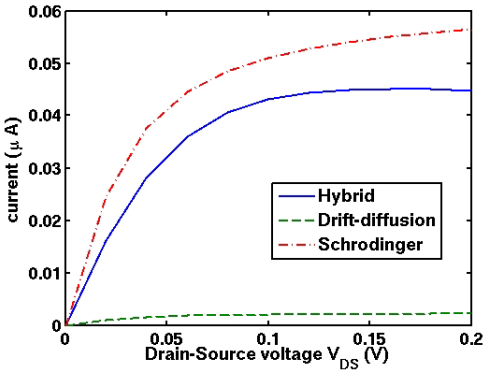

Figure 9: Comparison of the Current-Voltage characteristics between the three approaches for $\widetilde{\mu} = 0.5 \times 10^{-4}\ m^2\, V^{-1}\, s^{-1}$ and $V_G = -0.1$ V.

5.2 Hybrid results for the overlap and non-overlap cases

Now, we present the numerical results obtained with the hybrid approach. First, Fig.10 shows the 3D density for $V_{DS} = 0$ V and $V_G = -0.1$ V in the overlap case. This figure allows to visualize the formation of channels between Source and Drain. Also, we observe the atomic circular cross-section structure of the carbon nanotube, due to the incorporation of g_{nn}'s (presented in Figs.3-4).

Figs.11-12 represent the self-consistent potential for $V_{DS} = 0$ V in a 2D slice along the transport direction (x-axis in the pictures), cutting the cross-section in the middle. Fig.11 corresponds to a gate voltage $V_G = -0.1$ V, whereas Fig.11 corresponds to $V_G = 0.1$ V. We recover these values at top and bottom boundaries of the pictures (with the reverse sign since we plot energies expressed in eV). The overlap case is presented in the left figures and the non-overlap case in the right ones. In both cases, we observe a clear influence of the gate and of the doping. We detect also the cross-section structure of our device. Indeed, we recall that the external diameter of the CNT cross–section is 0.92 nm and so, at $z_1 \approx \pm 0.5$ nm, the different profiles have relevant variations. Electron channels are apparent between Source and Drain.

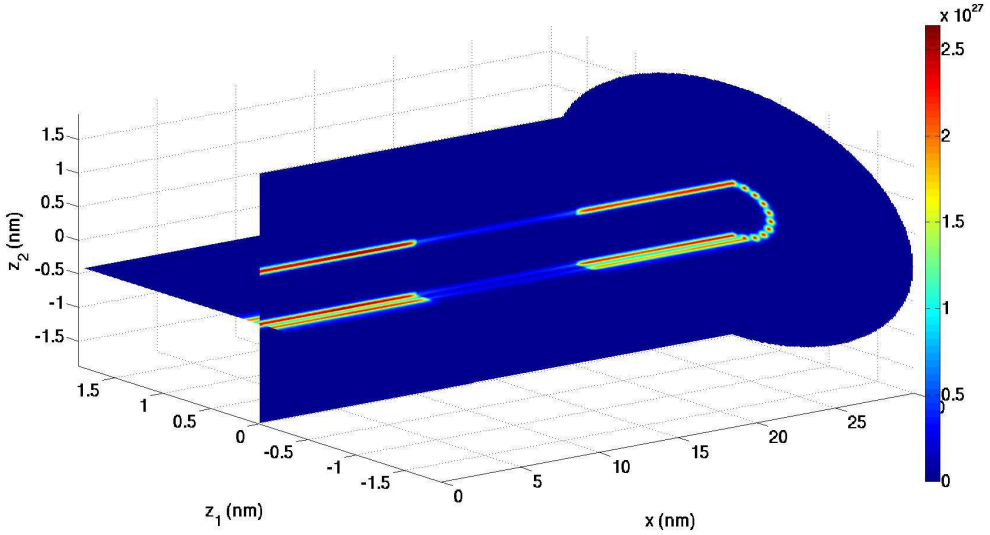

Figure 10: 3D density (m^{-3}) for $V_{DS} = 0$ V and $V_G = -0.1$ V.

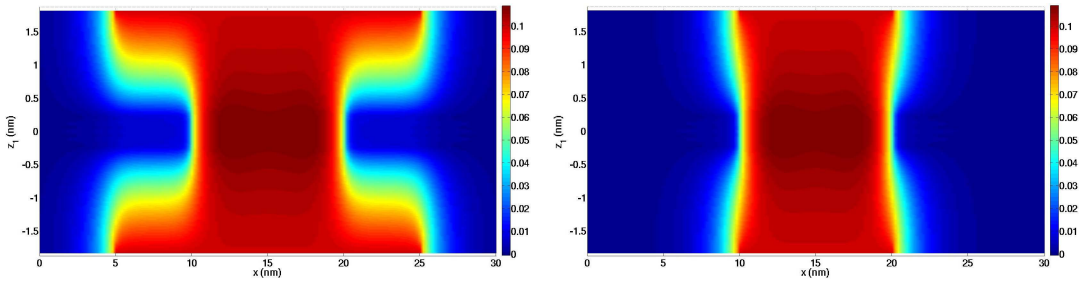

Figure 11: Potential energy (eV) for $V_{DS} = 0$ V and $V_G = -0.1$ V : overlap (left) and non-overlap (right) case.

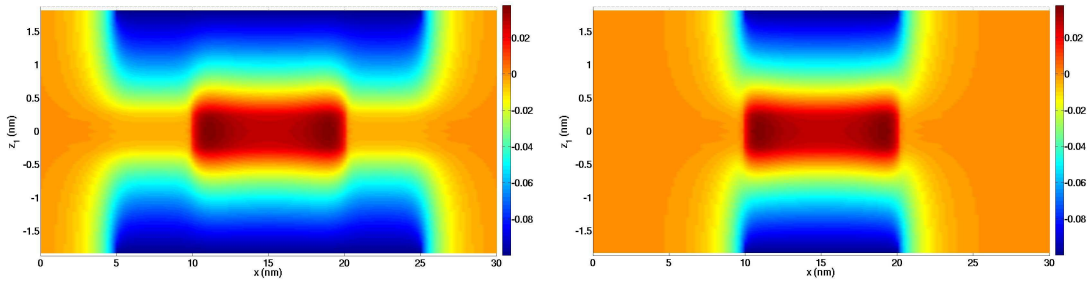

Figure 12: Potential energy (eV) for $V_{DS} = 0$ V and $V_G = 0.1$ V : overlap (left) and non-overlap (right) case.

1D profiles of the potential for $V_{DS} = 0$ V are presented for different gate voltages in Fig.13. These 1D curves are averaged quantities resulting from an integration of 3D quantities over the 2D wire section divided by the wire section surface. For low gate voltages, we observe that the potential in the channel has a value close to V_G, confirming that the transport is mainly controlled by the gate. Increasing the gate voltage, the channel potential energy always decreases but it does not reach V_G. In this case, the action of V_G on the potential in the active zone is governed by complex phenomena.

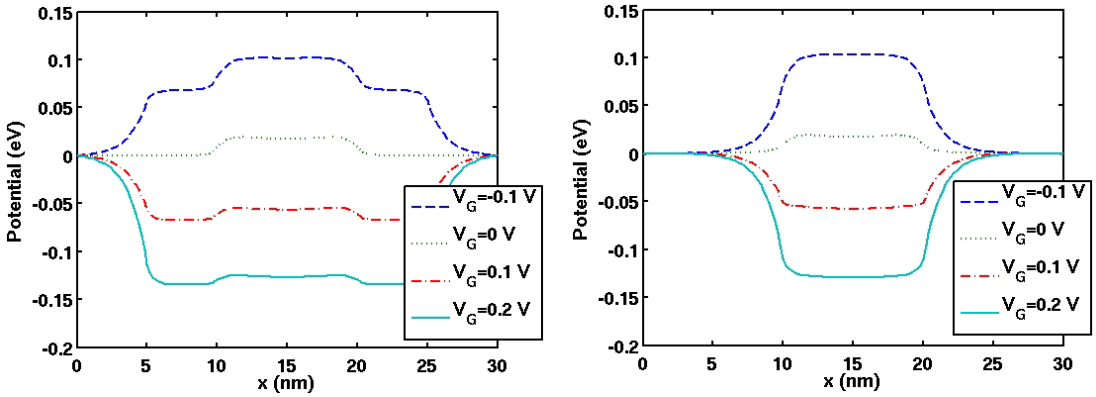

Figure 13: Averaged potential energy (eV) for $V_{DS} = 0$ V and for different V_G : overlap (left) and non-overlap (right) case.

Finally, in Fig.14, we represent the output characteristics for seven different gate voltages in the overlap case (similar behavior is obtained for the non-overlap case). The current in the CNTFET increases with the gate potential V_G. We notice the two typical regimes:

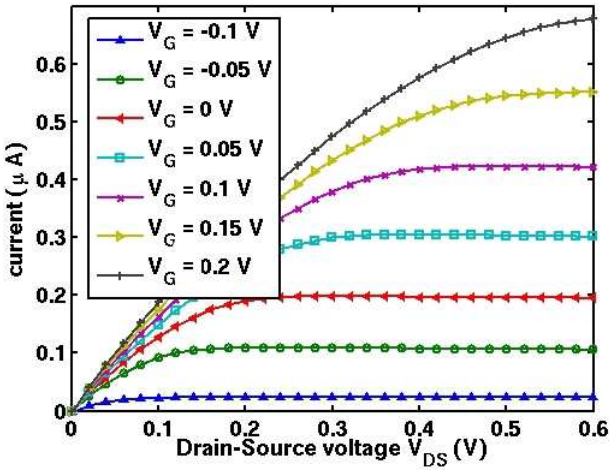

Figure 14: Current-Voltage characteristics for different gate voltages V_G.

an ohmic regime for values of Drain-Source voltage smaller than a threshold voltage V_{th} and a quasi-saturation regime for larger V_{DS}. The value of V_{th} increases with the gate potential. Indeed, for $V_G = 0$ V, V_{th} is about 0.2 V, instead for $V_G = 0.1$ V, it is about 0.4 V. All these results are in accordance with those reported in the literature for similar devices (see [14, 19, 26] e.g.).

5.3 Comparison of the three approaches

In this part, we shall compare the three approaches: full drift-diffusion model (dashed green curves in Figs.15–19), full quantum model (dashdotted red curves) and hybrid approach (solid blue curves). In Figs.15-16, 1D profiles of the potential are presented for $V_G = -0.1$ V, for $V_{DS} = 0$ V and for $V_{DS} = 0.2$ V, respectively. The same representation is done for 1D profiles of the density in Figs.17-18. As previously, the overlap case is presented in

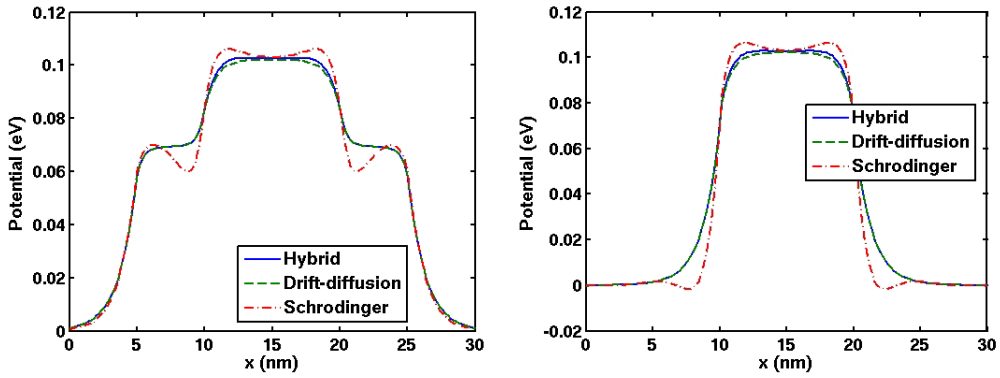

Figure 15: Comparison of the averaged potential energy (eV) for $V_{DS} = 0$ V and for $V_G = -0.1$ V : overlap (left) and non-overlap (right) case.

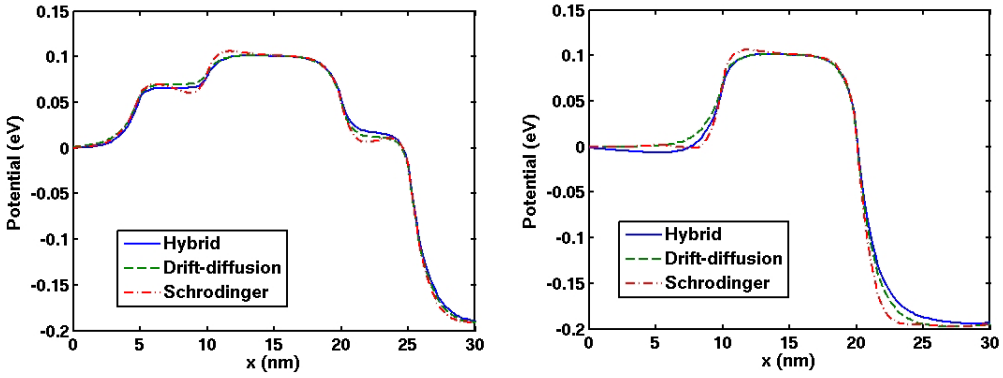

Figure 16: Comparison of the averaged potential energy (eV) for $V_{DS} = 0.2$ V and for $V_G = -0.1$ V : overlap (left) and non-overlap (right) case.

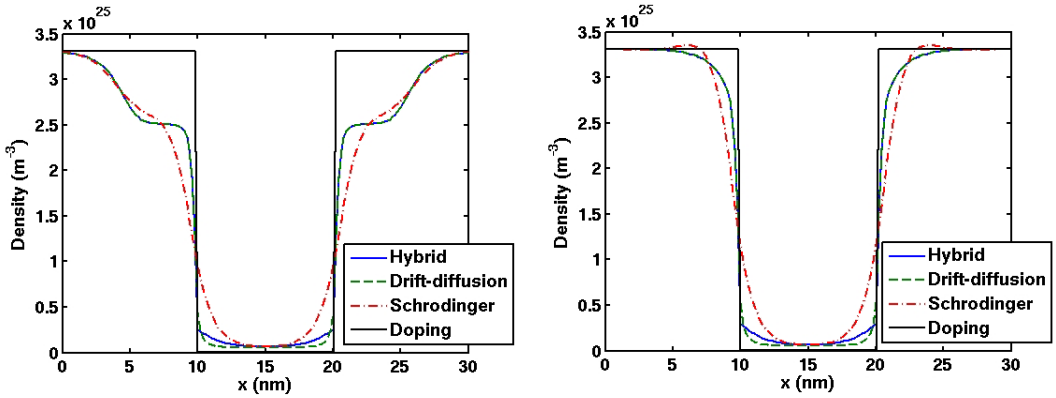

Figure 17: Comparison of the averaged density (m^{-3}) for $V_{DS} = 0$ V and for $V_G = -0.1$ V : overlap (left) and non-overlap (right) case.

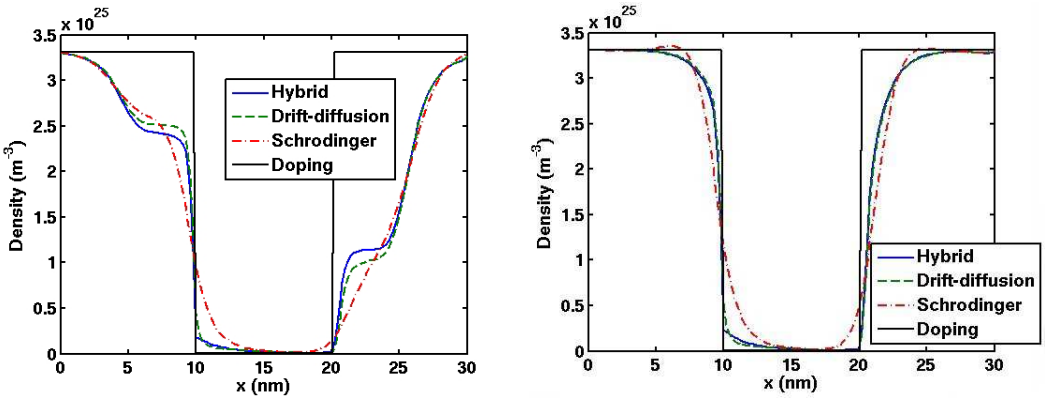

Figure 18: Comparison of the averaged density (m^{-3}) for $V_{DS} = 0.2$ V and for $V_G = -0.1$ V : overlap (left) and non-overlap (right) case.

the left figures and the non-overlap case in the right ones. The two cases exhibit similar behaviors. The differences between the three methods are mainly in the active zone and at the doping discontinuities. In these pictures, differences look rather small but this is mainly due to the scale of the plots. For a better comparison, it is interesting to plot average velocities, defined as $v(x) = J/[q \sum_n N_{1D}^n(x)]$. In Fig.19, they are calculated for $V_G = -0.1$ V and $V_{DS} = 0.2$ V. We observe three distinguishable curves, due not only to the different current values (see Fig.9), but also to the different densities. Moreover, for the hybrid approach, Fig.19 allows also to detect discontinuities of the density at the interfaces, which were not evident in Figs.17-18. We recall, that the interface conditions (3.31) and (3.32) enforce current continuity, but, as pointed out in Remark 3.1, density discontinuity may occur.

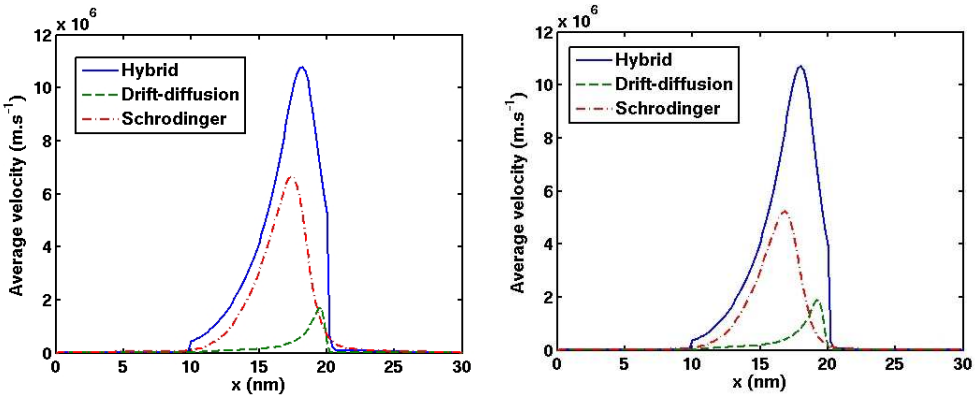

Figure 19: Comparison of the averaged velocity ($m.s^{-1}$) for $V_G = -0.1$ V and $V_{DS} = 0.2$ V : overlap (left) and non-overlap (right) case.

Now, we want to compare the full quantum model with the hybrid one from a computational point of view. The full drift-diffusion model is clearly cheaper, but, as we already mentioned, it does not take into account the relevant quantum effects that are essential in confined nanostructures. The total execution time necessary for computing a current-voltage characteristics curve at a fixed gate voltage (from $V_{DS} = 0$ V up to $V_{DS} = 0.2$ V) is approximatively 65% lower with the hybrid approach than with the quantum one. An obvious reason is that the quantum simulation, that requires the solution of a large number of Schrödinger equations at each iteration step, is performed on a smaller domain. Also, the hybrid method needs less Gummel iterations to reach convergence, as it is illustrated in Table 1. This is partly due to the boundary conditions since in the hybrid approach the quasi-neutral boundary conditions are imposed in a classical macroscopic manner. These numerical results aim at showing that our choice to use a hybrid approach including device dependent parameters allows for computationally efficient simulations.

		$V_G = -0.1\ V$		$V_G = 0.1\ V$	
		Schrödinger	Hybrid	Schrödinger	Hybrid
Nb. Gummel iterations	$V_{DS} = 0\ V$	37	10	46	20
	$V_{DS} = 0.02\ V$	28	5	31	13

Table 1: Number of Gummel iterations for the quantum model and the hybrid approach.

5.4 Interface positions

We now study the influence of the interface positions on the current. We remind that in the previous simulations the interfaces were located at $x_{I_1} = 10$ nm and $x_{I_2} = 20$ nm (at doping discontinuities). In Fig.20, we present the current value once the saturation regime

is reached. This test is run for $V_G = -0.1$ V in the overlap case. We point out that a similar dependence on the interface position occurs for different gate voltages and we do not report the pictures. In the left picture, x_{I_2} is fixed at 20 nm and we move x_{I_1}. Inversely, in the right picture, x_{I_1} is fixed at 10 nm and we move x_{I_2}. The dashdotted red line and the dashed green line correspond to the current value obtained, respectively, with the quantum and the drift-diffusion model in the entire longitudinal domain (without interfaces). In the two pictures, we observe a perceptible lowering of the current when one interface is placed well inside the active zone. It confirms that quantum ballistic effects play an essential role in the channel. However, moving the interfaces well inside the reservoirs, we observe two different behaviors. The current stays almost unchanged when the interface x_{I_2} goes to Drain, while the current increases up to the quantum value when the interface x_{I_1} reaches Source. This is not surprising since, once the saturation regime is established, the electrons flow almost unidirectionally from Source to Drain, and consequently in reservoirs it is the modeling of the electron transport (quantum ballistic vs classical collisional transport) in Source that is crucial to determine the current value.

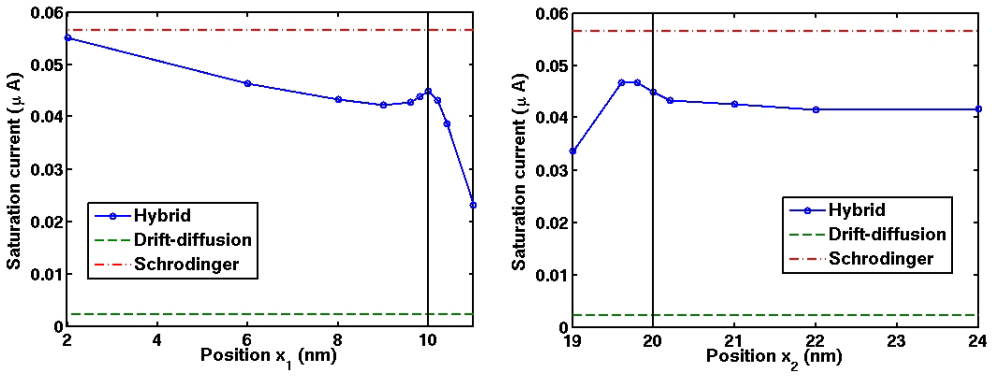

Figure 20: Current saturation obtained with the hybrid approach, moving the left interface position x_1 (left) and the right interface position x_2 (right) for $V_G = -0.1$ V.

5.5 Contribution of the different bands

Finally, we check that our initial choice of using only the 9 first conduction bands is relevant. In Table 2, we present the current distribution between the different bands for four different cases. In all cases, we see that only the two first bands give a significant contribution to the total current. This is due to the fact that for our (10,0) zig-zag single-walled CNT, the energy levels E_n increase quickly. Notice that in this table we can clearly recognize the multiplicity of the different E_n's.

		$V_G = -0.1\ V$		$V_G = 0.1\ V$	
		Overlap	Non overlap	Overlap	Non overlap
Current (μA)	1^{st} band	2.25×10^{-2}	2.36×10^{-2}	2.09×10^{-1}	2.12×10^{-1}
	2^{nd} band	2.24×10^{-2}	2.36×10^{-2}	2.08×10^{-1}	2.11×10^{-1}
	3^{rd} band	1.60×10^{-12}	1.69×10^{-12}	1.43×10^{-11}	1.48×10^{-11}
	4^{th} band	1.59×10^{-12}	1.68×10^{-12}	1.42×10^{-11}	1.47×10^{-11}
	5^{th} band	3.23×10^{-22}	3.40×10^{-22}	3.17×10^{-21}	3.29×10^{-21}
	6^{th} band	3.21×10^{-22}	3.38×10^{-22}	3.15×10^{-21}	3.27×10^{-21}
	7^{th} band	6.27×10^{-33}	6.62×10^{-33}	6.11×10^{-32}	6.36×10^{-32}
	8^{th} band	6.25×10^{-33}	6.60×10^{-33}	6.13×10^{-32}	6.34×10^{-32}
	9^{th} band	4.14×10^{-36}	4.37×10^{-36}	4.04×10^{-35}	4.20×10^{-35}
	Total	4.49×10^{-2}	4.72×10^{-2}	4.18×10^{-1}	4.23×10^{-1}

Table 2: Current distribution in the 9 first conduction bands.

6 Conclusion

In this paper, we propose a hybrid approach in the framework of strongly confined nanostructures. We spatially couple an effective mass Schrödinger system with a nanowire drift-diffusion model, preserving the current continuity. In these one dimensional transport models, the quantum confinement is taken into account averaging the effects of the two dimensional crystal structure. Simulations of a single-walled Carbon Nanotube Field-Effect Transistor aim at testing the capability of the approach to describe the electron transport with strong confinement. The reduced computational effort of this approach makes it suited for a device design framework.

Acknowledgements : Authors acknowledge partial support from the Galilée Project no 25992ND of the Hubert Curien program: *Modèles numériques du transport collisionnel dans des dispositifs nano-électroniques.*

References

[1] D. N. Arnold and F. Brezzi. Mixed and nonconforming finite element methods: implementation, postprocessing and error estimates. *RAIRO Modél. Math. Anal. Numér.*, 19(1):7–32, 1985.

[2] L. Barletti and N. Ben Abdallah. Quantum Transport in Crystals: Effective Mass Theorem and K·P Hamiltonians. *Comm. Math. Phys.*, 307:567–607, 2011.

[3] M. Baro, N. Ben Abdallah, P. Degond, and A. El Ayyadi. A 1d coupled Schrödinger drift-diffusion model including collisions. *J. Comput. Phys.*, 203(1):129 – 153, 2005.

[4] N. Ben Abdallah. A hybrid kinetic-quantum model for stationary electron transport. *J. Statist. Phys.*, 90(3-4):627–662, 1998.

[5] N. Ben Abdallah, P. Degond, and P. A. Markowich. On a one-dimensional Schrödinger-Poisson scattering model. *Z. Angew. Math. Phys.*, 48(1):135–155, 1997.

[6] N. Ben Abdallah, C. Jourdana, and P. Pietra. An effective mass model for the simulation of ultra-scaled confined devices. *Math. Models Methods Appl. Sci.*, 22(12):1250039, 2012.

[7] N. Ben Abdallah, C. Jourdana, P Pietra, and N. Vauchelet. A hybrid classical-quantum approach for ultra-scaled confined nanostructures : modeling and simulation. *ESAIM: Proc.*, 35:239–244, 2012.

[8] N. Ben Abdallah, F. Méhats, and N. Vauchelet. Diffusive transport of partially quantized particles: existence, uniqueness and long-time behaviour. *Proc. Edinb. Math. Soc. (2)*, 49(3):513–549, 2006.

[9] Ph. Caussignac, B. Zimmermann, and R. Ferro. Finite element approximation of electrostatic potential in one-dimensional multilayer structures with quantized electronic charge. *Computing*, 45(3):251–264, 1990.

[10] J.-C. Charlier, J.-P. Michenaud, and X. Gonze. First-principles study of the electronic properties of simple hexagonal graphite. *Phys. Rev. B*, 46:4531–4539, 1992.

[11] P. Degond and A. El Ayyadi. A coupled Schrödinger drift-diffusion model for quantum semiconductor device simulations. *J. Comput. Phys.*, 181(1):222–259, 2002.

[12] A. El Ayyadi and A. Jüngel. Semiconductor simulations using a coupled quantum drift-diffusion Schrödinger-Poisson model. *SIAM J. Appl. Math.*, 66(2):554–572, 2005.

[13] E. Gnani, A. Gnudi, S. Reggiani, M. Luisier, and G. Baccarani. Band effects on the transport characteristics of ultrascaled snw-fets. *IEEE Trans. Nanotechnol.*, 7(6):700 –709, 2008.

[14] E. Gnani, A. Marchi, S. Reggiani, M. Rudan, and G. Baccarani. Quantum-mechanical analysis of the electrostatics in silicon-nanowire and carbon-nanotube FETs. *Solid-state Electronics*, 50:709–715, 2006.

[15] H.K. Gummel. A self-consistent iterative scheme for one-dimensional steady state transistor calculations. *IEEE Trans. Electron Devices*, 11(10):455 – 465, 1964.

[16] F. Hecht and A. Marrocco. Mixed finite element simulation of heterojunction structures including a boundary layer model for the quasi-fermi levels. *COMPEL*, 13(4):757–770, 1994.

[17] F. Hecht, A. Marrocco, E. Caquot, and M. Filoche. Semiconductor device modelling for heterojunctions structures with mixed finite elements. *COMPEL*, 10(4):425–438, 1991.

[18] C. Jourdana and N. Vauchelet. Analysis of a diffusive effective mass model for nanowires. *Kinet. Relat. Models*, 4:1121–1142, 2011.

[19] S.O. Koswatta, Neophytos Neophytou, D. Kienle, G. Fiori, and M.S. Lundstrom. Dependence of DC characteristics of CNT MOSFETs on bandstructure models. *Nanotechnology, IEEE Transactions on*, 5(4):368–372, 2006.

[20] C. S. Lent and D. J. Kirkner. The quantum transmitting boundary method. *J. Appl. Phys.*, 67(10):6353–6359, 1990.

[21] A. Marchi, E. Gnani, S. Reggiani, M. Rudan, and G. Baccarani. Investigating the performance limits of silicon-nanowire and carbon-nanotube FETs. *Solid-state Electronics*, 50:78–85, 2006.

[22] P.A. Markowich, C.A. Ringhofer, and C. Schmeiser. *Semiconductor equations*. Springer-Verlag, Vienna, 1990.

[23] R. Martel, T. Schmidt, H. R. Shea, T. Hertel, and Ph. Avouris. Single- and multi-wall carbon nanotube field-effect transistors. *Appl. Phys. Lett.*, 73(17):2447–2449, 1998.

[24] A. Mayer. Band structure and transport properties of carbon nanotubes using a local pseudopotential and a transfer-matrix technique. *Carbon*, 42(10):2057 – 2066, 2004.

[25] P. Pietra and N. Vauchelet. Modeling and simulation of the diffusive transport in a nanoscale double-gate mosfet. *J. Comput. Electron.*, 7:52–65, 2008.

[26] M. Pourfath, H. Kosina, and S. Selberherr. Numerical study of quantum transport in carbon nanotube transistors. *Math. Comput. Simul.*, 79(4):1051–1059, 2008.

[27] R. Saito, G. Dresselhaus, and M. Dresselhaus. *Physical Properties of Carbon Nanotubes*. Imperial College Press, London, 1998.

[28] R. Saito, M. Fujita, G. Dresselhaus, and M. S Dresselhaus. Electronic structure of chiral graphene tubules. *Appl. Phys. Lett.*, 60(18):2204–2206, 1992.

[29] J. W. G. Wildöer, L. C. Venema, A. G. Rinzler, R. E. Smalley, and C. Dekker. Electronic structure of atomically resolved carbon nanotubes. *Nature*, 391:59–62, 1998.